Annu. Rev. Nucl. Part. Sci. 1999. 49:125–62

MEASUREMENT OF SMALL ELECTRON-BEAM SPOTS*

Peter Tenenbaum
Stanford Linear Accelerator Center, Stanford University, Stanford, California 94309; e-mail: quarkpt@slac.stanford.edu

Tsumoru Shintake
High Energy Accelerator Research Organization, Tsukuba, Japan; e-mail: tsumoru.shintake@kek.jp

Key Words linear accelerator, beam diagnostics, beam size, linear collider

■ **Abstract** Measurements of transverse beam size are tremendously important to the performance of e^+e^- linear colliders. In this paper we review the traditional technologies used to make such measurements, such as profile monitors and wire scanners, and their limitations. We introduce a new technique for electron beam-size measurement: Compton-scattered laser light, which may be used as an unbreakable "wire" or in the form of an interferometer beam-size monitor (BSM). We describe the use of such an interferometer BSM, noting both the general issues related to its design and operation and the specific experiences with such an interferometer at the Final Focus Test Beam at SLAC. We conclude by considering the ultimate limitations of the laser-interferometer BSM.

CONTENTS

1. Introduction 126
1.1 Emittance 126
1.2 Energy Spread 127
1.3 Interaction Point Parameters 128
1.4 Non-Gaussian Tails 128
2. Conventional Beam-Size Monitors 128
2.1 Profile Monitors 128
2.2 Wire Scanners 131
2.3 Beam-Beam Scans 132
3. Compton-Scattering Beam-Size Monitors 135
3.1 Quantitative Review of Compton Scattering 135
3.2 Example: The SLC/SLD Laser Wire 137

*The US Government has the right to retain a nonexclusive, royalty-free license in and to any copyright covering this paper.

4. Beam-Size Measurement Using Laser Interferometer 141
4.1 Systematic Effects 146
4.2 Laser-Interferometer Beam-Size Monitor in the Final Focus Test Beam 152
4.3 Use of the Laser-Interferometer Beam-Size Monitor at the FFTB 155
4.4 Ultimate Limits of Laser-Interferometer Beam-Size Monitor Technique 159
5. Conclusions 159

1. INTRODUCTION

Linear electron-positron accelerators have been used extensively to produce high-energy beams for fixed-target experiments (1, 2) and also as injectors into storage rings and synchrotrons (3–5). In these applications, the demands on linear accelerators (linacs) for production of very small, stable beams have not been severe. For example, the SLAC linac delivers a beam with a root-mean-squared (RMS) radial size of 0.5 mm to its fixed-target facility (1). Because the allowed beam sizes were so large, linacs historically were designed to deliver a beam whose size was large from the injector to the extraction point, and which was relatively insensitive to effects in the linac that would dilute the beam size.

More recently, linacs have been used for applications that demand smaller and more stable beams. For example, the Stanford Linear Collider (SLC) design required RMS beam sizes of 70 μm at the end of the linac (6). Future linear colliders envision beam sizes that are over an order of magnitude smaller. In addition, new injector technologies now permit generation of much smaller beams, and linac-driven free-electron lasers (FELs) demand extremely small beams at injection and excellent preservation of the small beam size (7). These requirements are much harder to achieve than the requirements for fixed-target and collider injection, and they cause high-performance linacs to be more sensitive to long-term instabilities.

Transverse beam-size measurements are an essential diagnostic tool for these high-performance linac applications. They are used for the initial tuning of the beamlines and for detection and correction of long-term instabilities. For example, at the SLC, beam-size measurements are performed at over 50 locations in the linac and beam delivery area (8), whereas the original SLAC linac, beam switchyard, and fixed-target facility contained only 12 beam-size diagnostic devices (1); the Final Focus Test Beam (FFTB) at SLAC measures the beam size at 7 locations (9). Future linear colliders are expected to have as many as 100 beam-size monitors, and the Linac Coherent Light Source (LCLS) design includes 25 beam-size monitors.

The uses of beam-size measurement can be divided into four general categories, which are described below.

1.1 Emittance

Linacs typically consist of radio-frequency (RF) accelerating structures interleaved with quadrupole magnets that focus the beam. Misaligned structures or quadrupoles can cause an increase in the beam size—the former through wakefields

(electric fields from the beam head deflecting the tail), the latter through dispersion (unequal deflection of particles of different energies by the magnetic field of the quadrupole). Either of these effects results in an increase in the incompressible phase volume of the beam, that is, the total area occupied by the particles of the beam in the (x, x') plane or the (y, y') plane, where x and y are the horizontal and vertical particle positions relative to the accelerator centerline, respectively, and x' and y' are the horizontal and vertical angles of the particle's trajectory relative to the accelerator centerline, respectively. In addition, many facilities including linear colliders rely on the acceleration of flat beams, in which one plane has a much smaller phase volume than the other. In such environments, cross-plane coupling from rotated quadrupole magnets can cause the smaller of the two phase volumes to be enlarged.

The deleterious effects of wakefields and dispersion are measured by fully reconstructing the size and shape of the beam phase space in x or y. The phase space typically takes the form of an ellipse in the (x, x') or (y, y') plane (10); thus, the phase space can be characterized by three independent parameters. The two parameterizations usually used are the independent second moments of the beam distribution ($\langle x^2 \rangle$, $\langle x'^2 \rangle$, and $\langle x x' \rangle$) or the emittance and Twiss parameters $(\epsilon, \beta, \alpha)$ (11). Although the two parameterizations are equivalent and each is easily translated to the other, the Twiss parameterization has the advantage of explicitly separating the incompressible phase volume, the emittance, from the parameters related to the orientation and aspect ratio of the ellipse.

The reconstruction of the beam ellipse in phase space requires measurement of three second moments of the beam at a given point in the accelerator, whereas beam-size measurement devices can only realistically measure the $\langle x^2 \rangle$ moment at a given point. Full emittance measurements require measuring the beam size at different betatron phase advances and using knowledge of the beam transport properties to reconstruct the second moments at a given point. The most common technique for this is to use a single beam-size monitor (BSM) and vary the strength of an upstream quadrupole; this changes the phase advance between the quadrupole's upstream face and the monitor (12). A less invasive technique is to use several monitors at different locations, and make a single measurement at each monitor; this permits reconstruction of the phase ellipse without changing any beamline magnet (13). This procedure is the preferred technique at modern high-performance linacs.

1.2 Energy Spread

Errors in klystron timing and phasing with respect to the beam can result in reduced energy gain and increased energy spread, which is usually unacceptable to any experiment to which beam from a linac is delivered (especially final focus systems of linear colliders and linac-driven FELs). The beam energy spread is measured by generating a strong correlation between transverse position and beam energy at a location in the beamline and measuring the transverse beam size. If the correlation (denoted by η or D and known as dispersion) is known and is large

enough that the dispersive beam size dominates the monochromatic beam size at the location, then the energy spread (and often the shape of the spectrum) can be calculated directly. Because it is often inconvenient to provide such a location, some knowledge of the beam's monochromatic size at the monitor's location is typically needed to deconvolute the data.

1.3 Interaction Point Parameters

The interaction point (IP) of a linear collider typically requires an extremely small spot size to provide adequate luminosity for the experiment. The SLC reduces beams to RMS sizes of 2.0 μm (horizontal) by 0.65 μm (vertical) (14). Future linear colliders may have spot sizes as small as 0.2 μm by 2.8 nm (15). Because the final focus systems for such colliders usually have strong aberrations that must be carefully corrected, direct measurement of the focused spot size is crucial to linear collider performance.

A related measurement is the beam angular divergence at the IP. This is determined by measuring the beam size at a point some distance from the IP, where the spot size is dominated by the divergence at the IP. The divergence measurement is important for two reasons. The first is background control; unacceptably large divergences result in the scattering of beam particles into the experimental detectors, which must be prevented to preserve data quality. The second is betatron matching. Although the IP beam size can be dominated by aberrations, the IP angular divergence is determined by linear beam optics. By knowing the beam divergence, θ^*, and the beam emittance, the betatron function at the IP, β^*, can be computed directly: $\theta^* = \sqrt{\epsilon/\beta^*}$. This measurement unambiguously determines whether an overlarge IP beam size is attributable to an optics mismatch or aberrations.

1.4 Non-Gaussian Tails

In addition to measuring the RMS transverse size of a beam distribution, many BSMs can measure higher moments. The most useful is the asymmetry of the beam profile, the third moment. Wakefields that deflect the downstream end of a bunch often result in profiles with a strong asymmetry, as shown in Figure 1. Although wakefield tails can be tuned by measuring the emittance, it is often more efficient to use a single BSM as the diagnostic signal for wakefield tuning strategies.

2. CONVENTIONAL BEAM-SIZE MONITORS

Because beam-size measurements are so widely used, several different techniques have been developed for performing the measurements. We describe some of the most widely applicable techniques below.

2.1 Profile Monitors

Figure 2 shows a schematic of a beam-profile monitor. An intercepting screen is inserted into the beam path at an angle of 45°; the emitted light is recorded

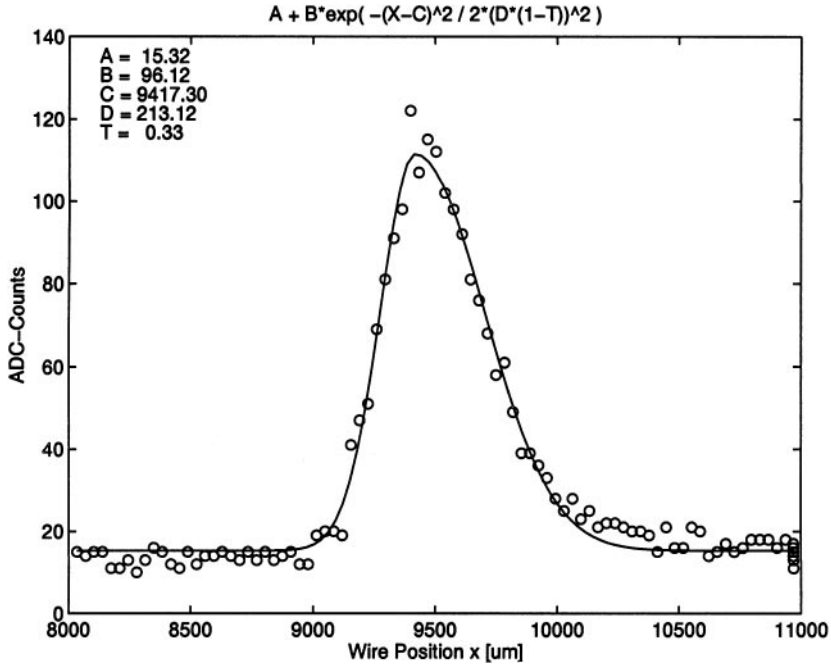

Figure 1 Example of a beam with a non-Gaussian transverse profile due to wakefields. The wakefields cause the particles at the tail end of the beam to be deflected to one side; as a result, that side of the transverse profile appears "wider." The beam in the figure has a 33% asymmetry and was measured with a wire scanner. Measured signal (circles) and asymmetric-Gaussian fit (solid) are shown.

by a camera and can thus be transported to a video display or a digitizer. In order to ensure that the screen emits light, phosphorescent coatings are usually employed (16); more recent profile monitors utilize optical transition radiation (17) or emission from yttrium-aluminum-garnet (YAG) crystals (18).

Profile monitors are almost always the simplest beam-size measurement devices. Consequently, even high-performance linacs have several profile monitors as the "diagnostic of last resort." A full horizontal/vertical profile can be produced by a single beam pulse, all details of the two-dimensional space distribution in the charge are preserved, and generally the image can be transmitted to a video screen (if not a digitizer) on every pulse, allowing observation of the evolution of the beam in real time.

However, profile monitors suffer from several disadvantages. Most obviously, they are destructive to the beam; a large fraction of the beam particles are scattered, and it is almost never possible to recapture and deliver a bunch that has passed through a profile monitor. Consequently, beam diagnostics that rely on profile monitors compete with delivery of beams to experimental areas, and they also cause irradiation of the surrounding equipment (including the profile monitor's camera,

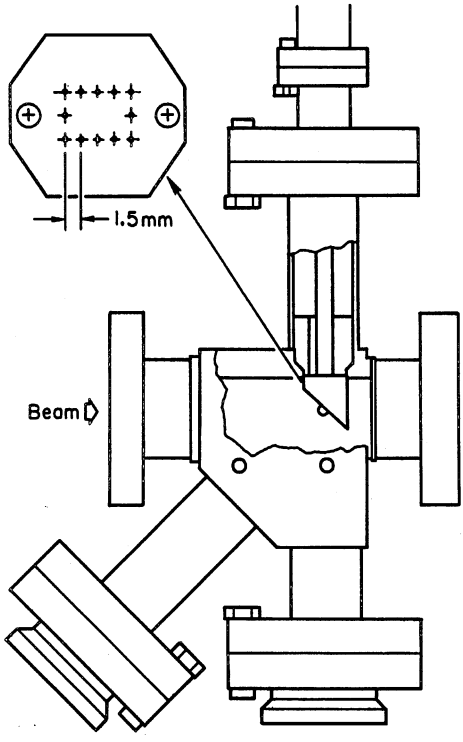

Figure 2 Schematic of a profile monitor. The beam passes through a sheet of material that emits light due to scintillation, transition or Čerenkov processes, or other effects. The screen is imaged by a camera and transported for viewing or to a digitizer.

a frequent cause of camera failure). Profile monitors are limited in their spatial resolution; phosphorescent screens are limited by the phosphor grain size to a typical resolution of 20 μm (19), and other profile monitors are limited by the optics of the light transport to the camera or the pixel size of the digitizer. Many profile monitors, especially phosphorescent screens, are limited in their temporal resolution by persistence of the emitted light. Finally, profile monitors are often limited in their dynamic range. A camera arrangement that produces a good image for small beams often is too diffuse to be digitized for large beams; conversely, if the profile monitor is set up properly for large beams, the image saturates for small beams.

Figure 3 shows one arrangement of profile monitors that reduces invasiveness. The profile monitors are off-axis from the accelerator, and a pulsed kicker deflects the beam onto the screens. A set of eight such screens is installed at the end of the SLAC linac; one electron pulse and one positron pulse is "stolen" for the screens by the kickers every 8 s (1 pulse out of 960, resulting in a 0.1% loss). The images from the screens are digitized and transmitted to the control room, resulting in a near-real-time display of the beam profile at the end of the linac (20).

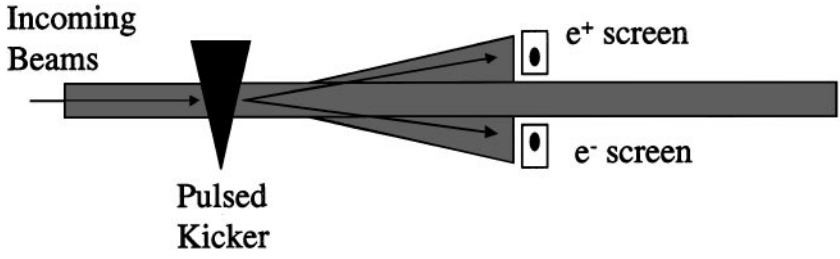

Figure 3 Noninvasive profile monitors used at the end of the SLAC linac. A pulsed kicker deflects the electron and positron beams onto separate off-axis screens; the images are digitized and transmitted to the control room. This technique allows profiles to be observed without inserting a screen into the path of the main beam.

2.2 Wire Scanners

Wire scanners, sometimes known as flying wires, are in common use at storage rings (21) and at linacs (22). Figure 4 shows a schematic. A yoke with one or more fibers (ranging in diameter from a few millimeters to a few microns) is attached to a translation stage, which is capable of moving the wire across the path of the beam. The intersection of the beam and the wire produces a shower of bremsstrahlung photons and scattered electrons, whose intensity is proportional to the amount of beam intercepted by the wire. If a detector is placed at an appropriate place, the measured intensity versus position looks like Figure 1, and the beam size and shape (in one dimension) can be directly reconstructed.

Wire scanners are substantially more difficult to use than profile monitors are. The scanner is a precision-stepped device rather than a simple in/out screen. A detector needs to be placed in an appropriate location (where the backgrounds are acceptable), provided with high voltage, and properly timed. The design of the wire scanner and its detector must be carefully optimized for the size and intensity of the beam. Furthermore, the wire scanner requires multiple pulses (or multiple turns in a storage ring) to generate a measurement. Because linacs are typically prone to pulse-to-pulse jitter, it is sometimes necessary to measure the beam position on each pulse and correct for changes.

Despite their many difficulties, wire scanners are the measurement tool of choice for most accelerators. One reason is that wire scanners are noninvasive; the actual fraction of the beam that is scattered is small, and therefore wire scanner operation usually does not interfere with beam delivery [although wire scanners close to detectors can produce unacceptable radiation (24)]. In addition, wire scanners are capable of much higher resolution than profile monitors. One limitation is the diameter of the wire. A wire that is round in cross-section has an RMS size equal to 25% of its diameter (9), which is added in quadrature with the beam size during measurement. Consequently, a wire with a 4-μm diameter cannot reliably measure a beam whose RMS size is smaller than 1 μm. However, this is a vast improvement

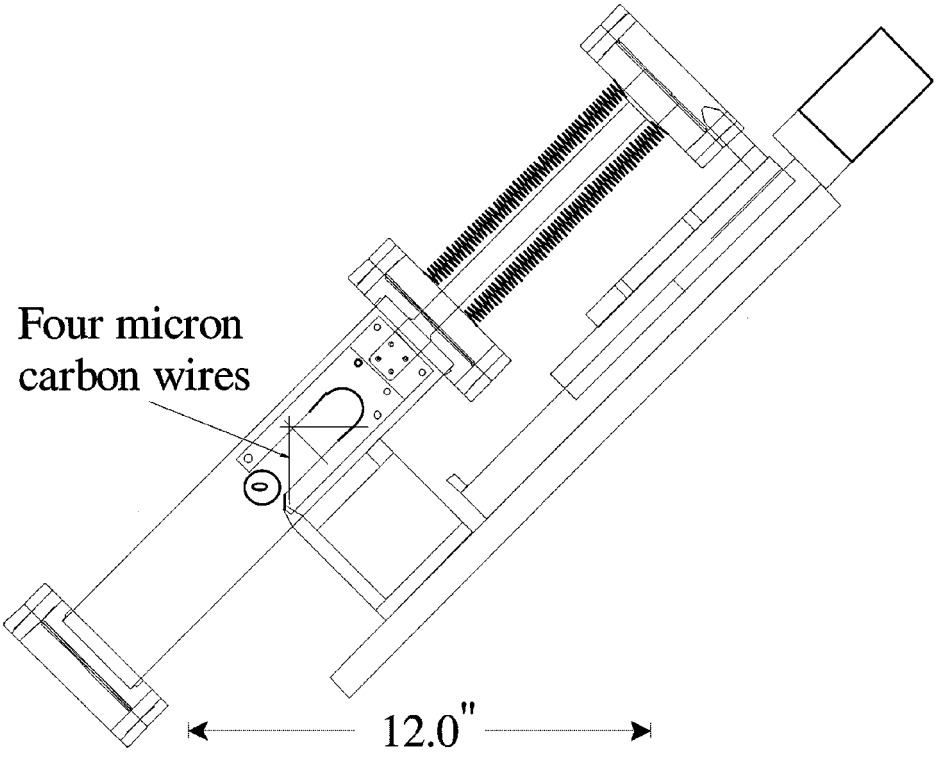

Figure 4 Diagram of a wire scanner.

over the capabilities of profile monitors, and wire scanners utilizing 4-μm wires are in common use today (23, 9). A further limitation is the step size of the wire translation stage; measurement of a 1-μm RMS beam size requires a stepper that can translate reliably in 0.3–0.5-μm steps.

In principle, a higher resolution is always achievable with a smaller wire size. Carbon and tungsten wires with diameters as small as 4 μm have been used; however, as the wire diameter is reduced, the strength of the wire is also reduced. A 4-μm carbon wire will be broken by an electron beam of 50 GeV if the ratio of the charge to the beam size, $N/(\sigma_x\sigma_y)$, exceeds 500 C m^{-2} (or in more practical terms, if the RMS transverse size for 3×10^9 electrons is smaller than 1 μm) (24). Smaller wires cannot be used for beam-size measurements except for bunches very low in charge. Novel techniques to get around this limit are being pursued, but for the time being, the stress limits restrict wire scanners to wires 4 μm in diameter or larger.

2.3 Beam-Beam Scans

At the IP of a collider, the beams are typically too small and intense to measure with wire scanners, and the constraints of the detector rarely allow such scanners.

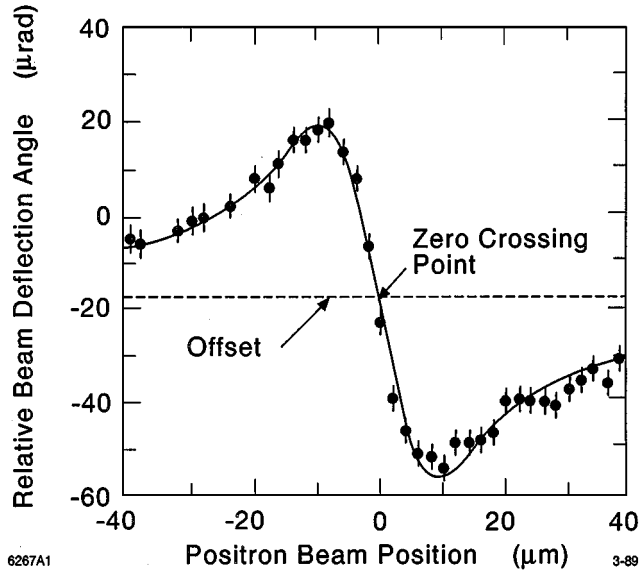

Figure 5 A beam-beam deflection scan. The deflection of one beam is plotted as a function of the separation of the two beams at the interaction point.

At such locations, the beam size is probed by looking at the beam-beam interaction itself.

Two properties of the beam-beam interaction are typically used for IP size measurements. The first is the deflection of one charged bunch by the other at small, nonzero distances. By stepping the position of one beam and measuring the deflection of the other (called a deflection scan), a measurement such as those in Figure 5 is obtained. The angle of the deflection is a function of the bunch charges, the separation, and the beam sizes (25), but in general, the slope of the central region of the scan (the region near head-on collisions) is proportional to either Σ_x or Σ_y, depending on whether a vertical or horizontal scan has been performed. The convolved beam size, Σ, denotes the quadrature sum of the sizes of the two colliding beams: $\Sigma_x^2 \equiv \sigma_{x1}^2 + \sigma_{x2}^2$, and $\Sigma_y^2 \equiv \sigma_{y1}^2 + \sigma_{y2}^2$. The second technique is to directly measure the luminosity[1] as a function of the separation between the two beams. In this case, one beam position is varied and the signal from a luminosity monitor is measured (Figure 6); the RMS width of the curve is equal to Σ_y. Deflection scans have been used at the SLC (26), PEP-II (27), and LEP (28); luminosity scans have been used at the SLC (29), PEP-II (27), and HERA (30).

[1]Luminosity is the approximate number of particle collisions produced by a collider per unit time, given the number of particles per bunch multiplied by the collision frequency, divided by the product of 4π times the horizontal and vertical RMS beam sizes.

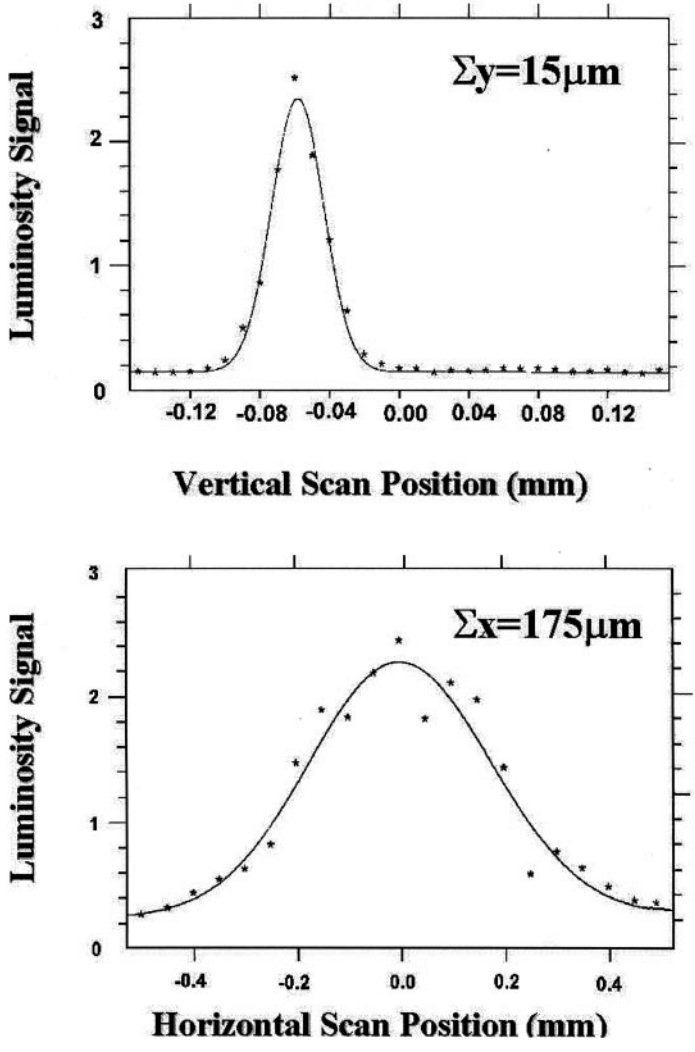

Figure 6 A beam-beam luminosity scan. The luminosity (in arbitrary units) is measured as a function of the beam separation at the interaction point, which is varied by a local beam deflection. The root-mean-squared (RMS) vertical width, 15 μm, and the RMS horizontal width, 175 μm, are the Σ_x and Σ_y at the interaction point, respectively.

Beam-beam scans do not have the limitations of wire scanners because there is no mechanical wire that can be broken and no apparatus consuming space in the particle physics detector. However, such measurements can only be made in places where the beams collide. Like wire scans, they require multiple bunches or multiple collisions of the same bunch, and often require jitter correction to be accurate. Deflection scans are sensitive to details in the model of the deflection; a mathematical model for round beams will not give correct beam sizes when the beams are quite flat, and disruption (the two beams focusing one another) adds further uncertainty to the model. Furthermore, because beam-beam scans only report Σ_x or Σ_y, they give no insight into which beam needs correction when the result is unacceptably large.

3. COMPTON-SCATTERING BEAM-SIZE MONITORS

A recent development in beam profiling has been the use of lasers to produce an indestructible target for intercepting the beam. This results in (*a*) a flux of Compton-scattered laser photons propagating downstream in the electron beam's path and (*b*) a flux of electrons with degraded energies from the collision, which may be deflected by a bending magnet and detected.

3.1 Quantitative Review of Compton Scattering

Extensively detailed studies of Compton scattering from ultra-relativistic electron beams have been published elsewhere (31–33; see also 34, whose general approach we follow here). We merely summarize their results as applied to the present problem.

Consider a laser beam with a power density ρ_L and frequency ν_0. The average photon density is given by

$$\langle n_0 \rangle = \frac{1}{ch\nu_0}\rho_L. \qquad 1.$$

The laser collides with an electron beam, of energy E and relativistic factor γ, at normal incidence. Photons from the laser are Compton scattered forward relative to the electron direction. If we assume that the laser power is uniformly distributed in z over a total distance D, the number of photons scattered out of the laser by collision with an electron beam containing N_e electrons is given by

$$\langle N_\gamma \rangle = \sigma_C \langle n_0 \rangle D N_e = \frac{\sigma_C}{ch\nu_0}\rho_L D N_e, \qquad 2.$$

where σ_C is the Compton-scattering cross-section. The Compton cross-section is related to the Thomson-scattering cross-section, $\sigma_0 \equiv 6.65 \times 10^{-25}$ cm^2,

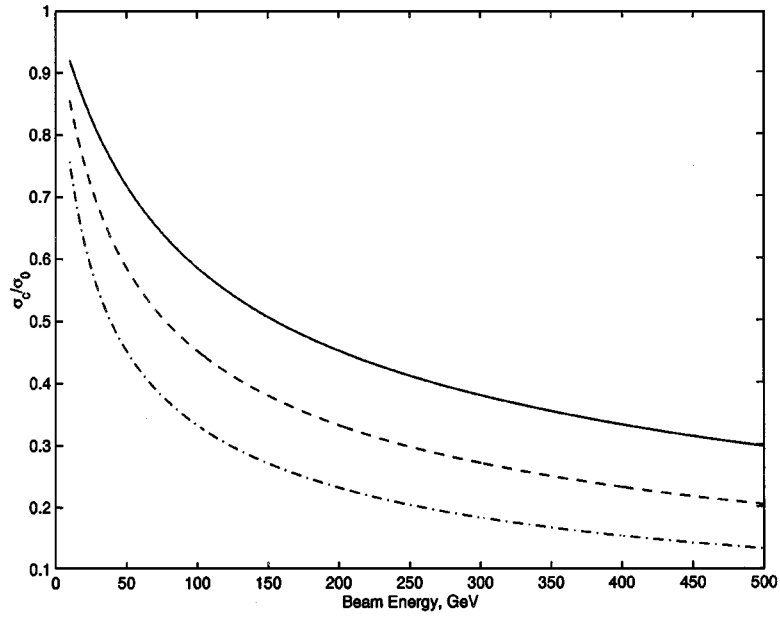

Figure 7 Ratio of Compton to Thomson cross-section, σ_c/σ_0, as a function of beam energy for a Nd:YAG laser operated at first (solid), second (dashed), or fourth (dot-dashed) harmonics.

by the relation

$$\frac{\sigma_{\mathrm{C}}}{\sigma_0} = \frac{3}{4}\left\{\frac{1+\epsilon_1}{\epsilon_1^3}\left[\frac{2\epsilon_1(1+\epsilon_1)}{1+2\epsilon_1} - \ln(1+2\epsilon_1)\right] + \frac{1}{2\epsilon_1}\ln(1+2\epsilon_1) - \frac{1+3\epsilon_1}{(1+2\epsilon_1)^2}\right\}, \qquad 3.$$

where $\epsilon_1 \equiv \frac{\gamma h\nu_0}{m_e c^2}$ is the normalized energy of the laser photons in the electron rest frame. Figure 7 shows the Compton cross-section, as a function of energy, for photons from a Nd:YAG laser ($\lambda = 1.064\ \mu$m) operated on first, second, or fourth harmonics. Note that for the case of head-on collisions between the laser photons and the electron beam, the normalized photon energy in the electron rest frame is doubled and the cross-section is reduced.

The energy spectrum of the emerging photons is given by

$$\frac{\mathrm{d}\sigma/\sigma_0}{\mathrm{d}w} = \frac{3}{8\epsilon_1}F(\epsilon_1, w), \qquad 4.$$

where $w \equiv h\nu_\gamma/E$ is the energy of the emitted photon normalized to the electron

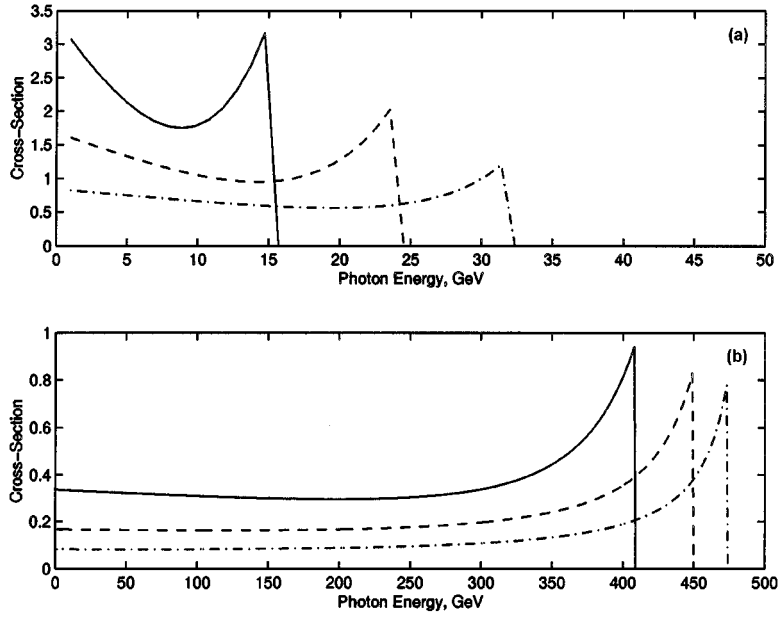

Figure 8 Spectrum of Compton-scattered photons from a 50-GeV (*top*) or 500-GeV (*bottom*) electron beam. The spectrum is shown for a Nd:YAG laser at first (solid), second (dashed), or fourth (dot-dashed) harmonics.

energy, and F is given by

$$F(\epsilon_1, w) = \frac{1}{1-w} + 1 - w + \left[\frac{w}{\epsilon_1(1-w)}\right]^2 - \frac{2w}{\epsilon_1(1-w)}. \qquad 5.$$

The maximum photon energy is given by $h\nu_{\max} = 2E\epsilon_1/(1+2\epsilon_1)$. Figure 8 shows the spectrum for first, second, and fourth harmonics of Nd:YAG laser photons scattered from 50-GeV and 500-GeV electrons.

The critical angle of emitted radiation is given by

$$\alpha_c = \frac{\sqrt{1+2\epsilon_1}}{\gamma}. \qquad 6.$$

The emitted photons are generally confined to a cone whose half-angle is a few times α_c.

3.2 Example: The SLC/SLD Laser Wire

The most straightforward use of Compton-scattered laser light for beam profiling is the SLC/SLD laser wire (35). In this case, a laser propagating perpendicular to the electron beam is focused to a diffraction-limited waist, and the electron

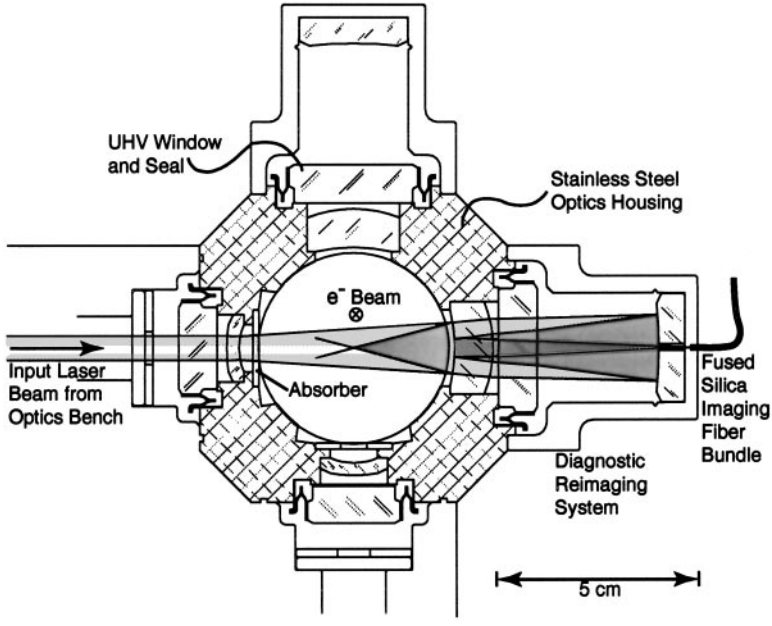

Figure 9 Schematic of SLC/SLD interaction-point laser wire. Light enters at left, is focused by a spherical mirror on the right, and collides with the electron beam in the center. Approximately 1% of the laser power is transmitted through the focusing mirror and reimaged for diagnostic purposes on the far right. The scan is performed by transverse motion of the beam via upstream corrector magnets.

beam is brought into collision with the laser beam at the waist. The electron beam is scanned in position across the laser beam, and the Compton-scattered photons and/or degraded electrons are collected downstream; a plot of detected photons/electrons versus electron beam position reveals the size of the electron beam. The laser beam can be viewed as a wire scanner with an unbreakable and extremely narrow wire.

Figure 9 shows a diagram of the laser-wire beamline apparatus. A parallel laser beam [third-harmonic yttrium-lithium-fluoride (YLF), $\lambda = 350$ nm] is transported to the apparatus, crosses the beam path, and is reflected by a focusing mirror. The spent light is then absorbed by glass absorbers. This arrangement permits 1% of the laser light to be transmitted through the focusing mirror and imaged for diagnostic purposes. In addition, because the incoming light fills a significant fraction of the beampipe, it is easier to locate with the electron beam than the light at the laser focus; this permits an unfocused electron beam to be used to adjust the collision timing with the laser.

In order to measure small electron spots, the waist of the laser must be smaller than the smallest anticipated electron beam size. At the same time, the depth of the focus should be relatively large, so that the sensitivity of the vertical size

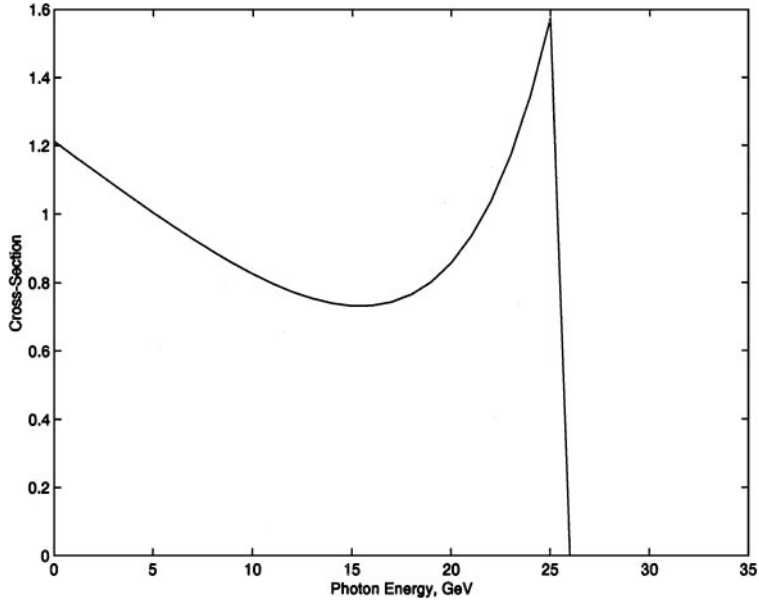

Figure 10 Spectrum of Compton-scattered photons from the SLC/SLD laser wire.

measurement to the horizontal position of the beam is minimized. These two constraints, coupled with the space limitations of the installation, set most of the critical parameters of the design.

The minimum transverse RMS size of a diffraction-limited laser beam is

$$\sigma_{\mathrm{f}} = \frac{\lambda f}{4\pi\sigma_{\mathrm{in}}}, \tag{7.}$$

where f is the focal length of the lens and σ_{in} is the RMS size of the incoming laser beam. In practice, the value of σ_{in} is limited by the acceptance of the laser transport and of the focusing mirror, and f is limited by the aperture of the beampipe. The Rayleigh range is defined as the distance over which a focused laser beam diverges to $\sqrt{2}$ times its final size, and is given by

$$z_{\mathrm{R}} = \frac{4\pi\sigma_{\mathrm{f}}^2}{\lambda}. \tag{8.}$$

In order to simultaneously achieve $\sigma_{\mathrm{f}} < 400$ nm and $z_{\mathrm{R}} \geq 5$ μm in the space allowed, it is necessary to select the near-UV third-harmonic YLF laser.

For a 45.6-GeV electron beam and 350-nm laser wavelength, the spectrum of emitted photons is shown in Figure 10, and the peak photon energy is 25 GeV. If we consider a vertical scan, the number of photons emitted as a function of the vertical beam position is given by

$$\langle N_\gamma \rangle = \frac{P_{\mathrm{L}}\sigma_{\mathrm{C}}}{ch\nu_0} \frac{1}{\sqrt{2\pi}\sigma_s} \exp\left(\frac{-y^2}{2\sigma_s^2}\right) \int_{-\infty}^{\infty} dz \frac{1}{\sqrt{2\pi}\sigma_{\mathrm{f}}} \exp\left(\frac{-z^2}{2\sigma_{\mathrm{f}}^2}\right), \tag{9.}$$

where we have written the power density in terms of the laser power P_L and assumed the laser power is Gaussian-distributed in y and z, and where σ_s is the overlap size of the electron beam and laser beam at the waist, $\sigma_s^2 \equiv \sigma_y^2 + \sigma_f^2$. If we assume a vertical RMS electron beam size of 1 μm and the laser parameters stated above, the Compton cross-section is 3.47×10^{-25} cm^2, and the expected number of photons at the laser waist is approximately 8000 for a peak laser power of 10 MW. Note that this is a slight overestimate; the beam has a horizontal RMS size of a few microns, which means that some particles are displaced from the laser waist and encounter a correspondingly lower photon density. This effect is on the order of 10%. The photon critical angle is 17 microradians, whereas the electron beam divergence is typically close to 300 microradians.

The beams exiting from the SLC IP enter the opposing final focus system, which contains several strong bending magnets. This allows the primary beam to be separated from the 25-GeV photon beam and the 20-GeV scattered electrons. The intensity of either electrons or photons may be recorded for the BSM. Figure 11 shows a measurement of the beam size using degraded electrons for the signal.

It is worth noting that, for a physically realizable installation, the minimum achievable laser waist (and therefore the smallest beam size measurable) is comparable to the laser wavelength. The beams at future linear colliders will be much more intense at the IP than SLC's [with up to 10^{12} particles per machine pulse and typical linac beam sizes from 1 to 10 μm (36)], and it is anticipated that laser wires will be the standard BSM for most locations. However, laser wavelengths

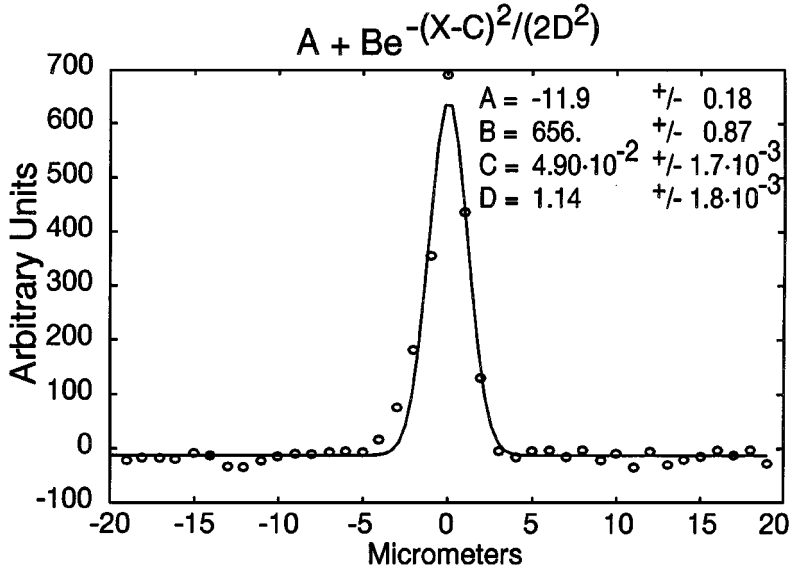

Figure 11 Measurement of the beam transverse size with a laser wire. The measured beam size is approximately 1 μm.

below 250 nm (fourth-harmonic YAG or YLF) will be difficult or impossible to achieve with the reliability required for beam diagnostics, and so, for spot sizes smaller than 250 nm, other approaches must be used.

4. BEAM-SIZE MEASUREMENT USING LASER INTERFEROMETER

Figure 12 illustrates the general principle of laser-interferometric beam-size measurements. A single laser beam is introduced into a resonant cavity, resulting in a standing-wave pattern in the electromagnetic field (34). The fringe spacing of the standing-wave pattern is half the wavelength of laser light used; a first-harmonic YAG laser, $\lambda = 1064\ \mu$m, generates a pattern with 532-nm spacing.

Now consider an electron beam that is scanned across the standing-wave pattern. If the beam size is large relative to the fringe spacing, the core of the beam always intercepts several nulls and peaks of the interference pattern; consequently, the number of photons that the beam will Compton scatter is only a weak function of the electron beam position. If the beam size is very small relative to the fringe spacing, the number of Compton-scattered photons is a strong function of the electron beam position—for an infinitely small beam, the maximum number of photons are scattered when the beam intercepts a bright fringe, whereas no photons are scattered when the beam intercepts a null. In general, the number of scattered photons as a function of position is given by $\langle N_\gamma \rangle = A + B\cos(2k_{\mathrm{L}}x + \psi)$, where k_{L} is the laser wave number and ψ an arbitrary constant. The ratio B/A

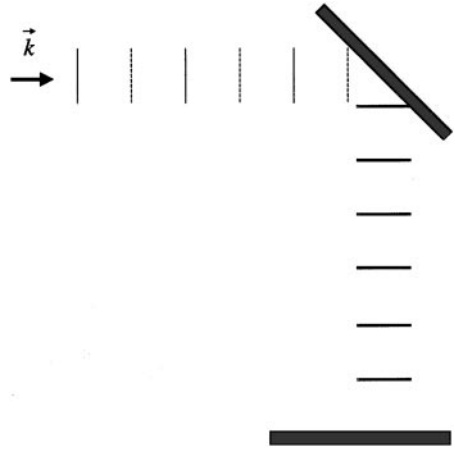

Figure 12 Diagram of simple laser interferometer for beam size measurement. A laser with wave vector $\vec{k}$ is introduced into a resonant cavity. The resulting standing-wave pattern has intensity maxima (dark solid lines) whose spacing is half the wavelength of the incoming laser (solid lines, maxima; dashed lines, minima).

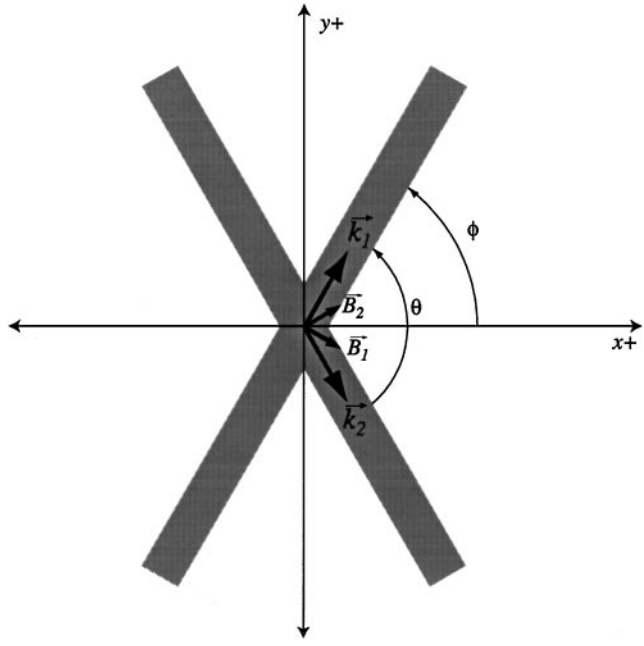

Figure 13 Diagram of two lasers intersecting at an angle θ; the magnetic field vectors ($\vec{B}_1$ and $\vec{B}_2$) and momentum vectors ($\vec{k}_1$ and $\vec{k}_2$) are shown.

is known as the modulation depth, and is zero for an infinitely large beam and 1 for an infinitely small beam, as shown in Figure 14. It therefore follows that the modulation depth is a function of the beam size and that the beam size may be inferred from a measurement of the modulation depth.

The system sketched in Figure 12 is not practical for several reasons, one of which is that the fringe spacing is always equal to half the wavelength of light selected. If the beam is too large or too small to be well measured by the system, the laser wavelength must be changed, which is not practical. Consider instead a system in which the incoming laser beam is split, and half the laser power is introduced into the interaction region at an angle $+\phi$ relative to the horizontal, while the other half is introduced at an angle $-\phi$ (Figure 13) (37). If the wavenumber of the laser is given by k and the polarization of the laser is such that the magnetic field is in the xy plane while the electric field is parallel to the electron path (along z), then

$$\begin{aligned} \vec{k}_1 &= k(\hat{x}\cos\phi + \hat{y}\sin\phi), \\ \vec{k}_2 &= k(\hat{x}\cos\phi - \hat{y}\sin\phi), \end{aligned} \qquad 10.$$

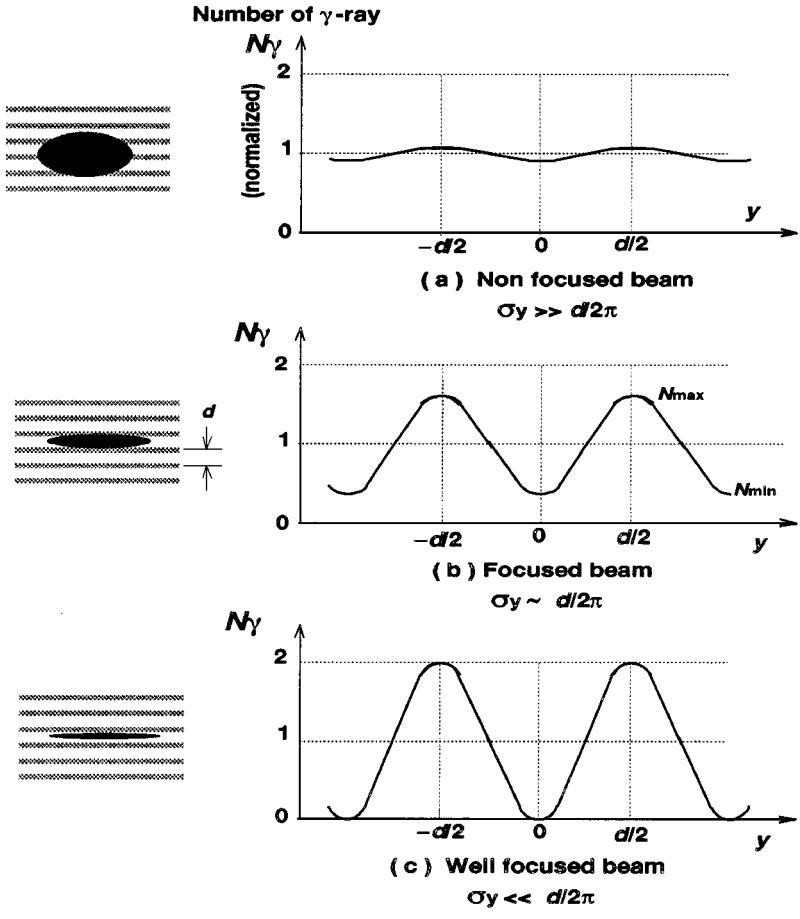

Figure 14 Use of laser-interferometer to measure a beam size. A beam that is large relative to the fringe spacing does not produce modulation in the intensity of Compton-scattered photons as it is scanned across the interference pattern (*top*); a beam that is very small relative to the fringe spacing produces nearly 100% modulation (*bottom*).

while the magnetic field vectors of the two beams are given by

$$\vec{B}_1 = B\cos(\omega t - \vec{k}_1 \cdot \vec{r})\,\hat{B}_1,$$
$$\vec{B}_2 = B\cos(\omega t - \vec{k}_2 \cdot \vec{r})\,\hat{B}_2,$$
$$\hat{B}_1 = \hat{x}\sin\phi - \hat{y}\cos\phi,$$
$$\hat{B}_2 = -\hat{x}\sin\phi - \hat{y}\cos\phi. \qquad 11.$$

The vector sum $\vec{B}_1 + \vec{B}_2$ is

$$\vec{B}_1 + \vec{B}_2 = 2B[\hat{x}\sin\phi\sin k_y y\sin(\omega t - k_x x) + \hat{y}\cos\phi\cos k_y y\cos(\omega t - k_x x)], \tag{12.}$$

where we have replaced $k\cos\phi$ with k_x and $k\sin\phi$ with k_y. Equation 12 shows that the interference of the two laser beams produces a standing-wave pattern in the vertical and a traveling wave in the horizontal, and it also shows that the periodicity of the standing-wave pattern is controlled by k_y, which is in turn a function of the crossing angle of the two beams. By varying the crossing angle, therefore, it is possible to change the fringe spacing of the interference pattern and tune the pattern to measure beams of various sizes.

Equation 12 can be used to compute the value of $\langle B_x^2 + B_y^2\rangle$ as a function of y. Because the wave is a traveling wave in the horizontal, we can replace all $\sin^2(\omega t - k_x x)$ and $\cos^2(\omega t - k_x x)$ terms with 1/2, leaving

$$\begin{aligned}\left\langle B_x^2 + B_y^2\right\rangle &= B^2[\sin^2 k_y y(1 - \cos 2\phi) + \cos^2 k_y y(1 + \cos 2\phi)] \\ &= B^2(1 + \cos 2\phi\cos 2k_y y).\end{aligned} \tag{13.}$$

Equation 13 shows that the fringe spacing will be given by $d \equiv \pi/k_y = \lambda_L/2\sin\phi$. For head-on laser collision, $\phi = \pi/2$, and the spacing reduces to the familiar form for pure standing waves, whereas for smaller crossing angles the fringe spacing increases. Note, however, that the maximum modulation depth in Equation 13 is $\cos 2\phi$. Thus, for head-on collisions, the modulation depth of the fringe pattern is 100%, whereas for the special case of perpendicular laser beams ($\phi = \pi/4$), the wave is a traveling wave and no modulation is possible.

We can quantify the relationship between beam size and Compton-scattering modulation depth by convolving Equation 13 with the charge distribution of a Gaussian beam, RMS size σ_y, centered at position y_0:

$$N_\gamma \propto \int_{-\infty}^{+\infty} \frac{1}{\sqrt{2\pi}\sigma_y}\exp\left[\frac{-(y - y_0)^2}{2\sigma_y^2}\right](1 + \cos\theta\cos 2k_y y)\,dy, \tag{14.}$$

where we have used the full crossing angle, θ, in place of 2ϕ. Integrating this equation and replacing the average number of photons with N_0 results in (38)

$$N_\gamma(y_0) = \frac{N_0}{2}\left\{1 + \cos 2k_y y_0\cos\theta\exp\left[-2(k_y\sigma_y)^2\right]\right\}. \tag{15.}$$

The maximum and minimum numbers of Compton-scattered photons are denoted as N_+ and N_-:

$$\begin{aligned}N_+ &= N_0/2(1 + \cos\theta\cdots), \\ N_- &= N_0/2(1 - \cos\theta\cdots).\end{aligned} \tag{16.}$$

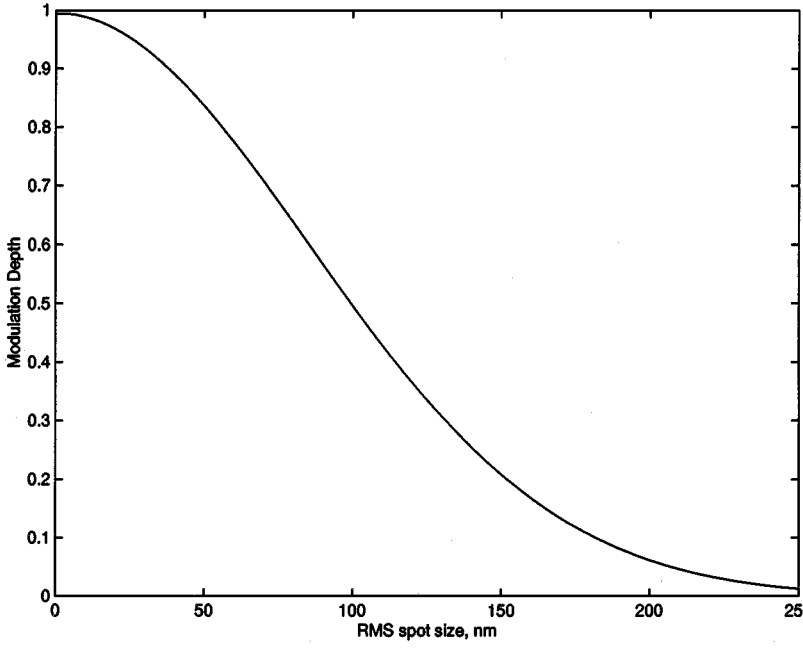

Figure 15 Modulation depth as a function of beam size for laser-interferometer beam-size monitor with laser crossing angle of 174°. The range of the monitor is from 40 nm to 180 nm.

The ratio of the oscillation in Compton rate to the average rate, M, is

$$M \equiv \frac{N_+ - N_-}{N_+ + N_-} = |\cos\theta| \exp\left[-2(k_y\sigma_y)^2\right]. \quad 17.$$

From Equation 17, we can estimate the spot size from the measured modulation depth:

$$\sigma_y = \frac{d}{2\pi}\sqrt{2\ln\left(\frac{|\cos\theta|}{M}\right)}. \quad 18.$$

Figure 15 shows the modulation depth as a function of the beam size for a first-harmonic Nd:YAG laser with a crossing angle of 174° ($d = 533$ nm). The largest beam that can reasonably be measured (at a modulation depth of 10%) is $\sigma_y = 182$ nm, and the smallest beam that can be measured ($M = 90\%$) has an RMS size of 38 nm. At the other extreme, a crossing angle of 6° can measure beam sizes from 3.5 μm down to 730 nm, with a 10.2 μm fringe spacing.

4.1 Systematic Effects

One of the useful features of the laser-interferometer technique is that most (though not quite all) of the systematic effects tend to reduce the modulation depth, usually by increasing the number of Compton scatters that occur at a nominal null (through imperfections in the fringe pattern). Thus, the measured beam size is usually an overestimate of the actual beam size. Several of the most important effects are discussed below.

4.1.1 Laser Power Imbalance Heretofore we have assumed that the laser power in the two interferometer arms is equal. If the power to the two arms is imbalanced, then the total fringe modulation is reduced. If the power in the two arms is given by P_1 and $P_2 \equiv P_1 P_\mathrm{I}$, then Equation 17 can be modified to show that

$$\begin{aligned} M &= C_\mathrm{P} |\cos\theta| \exp\left[-2(k_y\sigma_y)^2\right] \\ &= C_\mathrm{P} M_\mathrm{ideal}, \end{aligned} \tag{19.}$$

where P_I is the relative power-imbalance factor and C_P is the correction factor for the total modulation depth of the interference pattern:

$$C_\mathrm{P} = \frac{2\sqrt{P_1 P_2}}{P_1 + P_2} = \frac{2\sqrt{P_\mathrm{I}}}{1 + P_\mathrm{I}}. \tag{20.}$$

Figure 16 shows the value of C_P as a function of P_I. The correction to the fringe modulation is not a strong function of the power imbalance; an imbalance of a factor of 2 results in a loss of only 6.1% in the pattern modulation depth. The resulting error in beam-size estimate is

$$\frac{\delta\sigma_y}{\sigma_y} = \left(\frac{d}{2\pi\sigma_y}\right)^2 \frac{\delta C_\mathrm{P}}{C_\mathrm{P}}. \tag{21.}$$

The error resulting from the experimental uncertainty in the power imbalance is a strong function of the measured beam size itself. For a 2% error in C_P, a 60-nm beam size measured in the apparatus described above is overestimated by 4%, whereas a 75-nm beam size is overestimated by only 2.6%.

4.1.2 Electron Beam Crossing Angle If the trajectory of the electron beam is not parallel to the plane of the fringes, as shown in Figure 19, the beam will pass through the interference pattern at an angle. In this case, the modulation in the Compton-scattered photons is reduced and the apparent beam size is increased. For a crossing angle α, the apparent increase in measured beam size is given by

$$\sigma_\mathrm{meas}^2 = \sigma_y^2 + \alpha^2\sigma_z^2, \tag{22.}$$

where σ_z is the RMS longitudinal size of the laser.

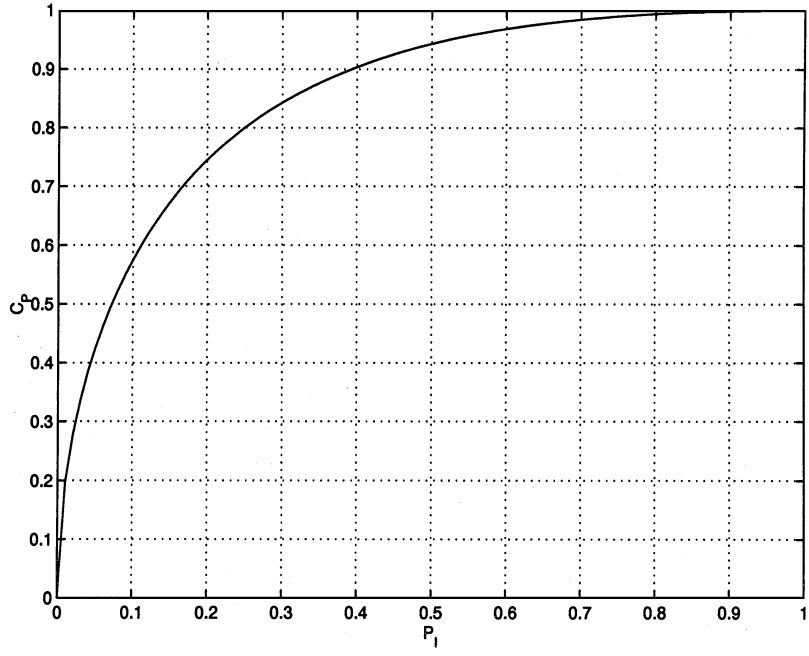

Figure 16 Relationship between power imbalance factor, P_l, and fringe contrast, C_P. Perfectly balanced laser power in the two interferometer arms corresponds to $P_l = 1$. C_P is a weak function of P_l; a 2:1 power imbalance results in a reduction in contrast of only 6%.

4.1.3 Longitudinal Extent of Interference Pattern The interference pattern formed by the laser has a nonzero longitudinal extent, and although most photons are Compton scattered at the core of the pattern, where the intensity is highest, some scatter off the upstream and downstream ends of the interference pattern. If the beam size at the core is not equal to the beam size at the extremes, there will be some averaging over the different regions.

As one example, consider the situation in Figure 18. The electron beam's waist is at the z location of peak laser intensity, but the beam divergence causes the beam to be larger at the upstream and downstream ends of the pattern. In this case, to good approximation, the measured beam size σ_{meas} is related to the actual beam size σ_y, the RMS laser size σ_z, and the RMS electron beam divergence $\sigma_{y'}$, as follows:

$$\begin{aligned}\sigma_{\text{meas}}^2 &\approx \sigma_y^2 + \sigma_{y'}^2\sigma_z^2 \\ &= \sigma_y^2 + \left(\frac{\sigma_y}{\beta_y^*}\right)^2 \sigma_z^2, \end{aligned} \tag{23.}$$

where β_y^* is the vertical betatron function at the focal point of the electron beam.

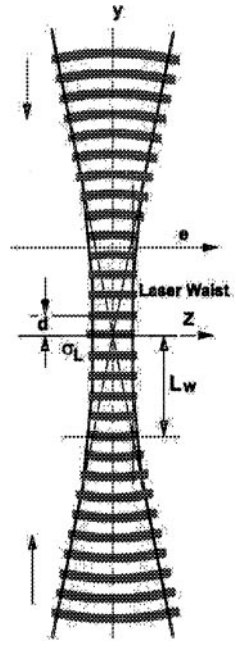

Figure 17 Diagram of spherical wavefront error. The wavefronts of a focused laser are only planar to good approximation within a fraction of the Rayleigh range.

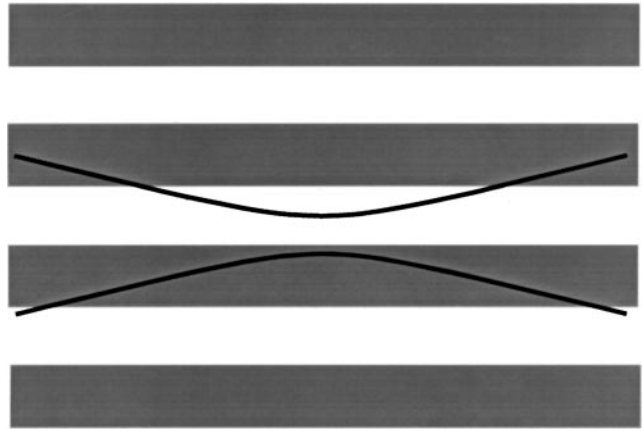

Figure 18 Overlap of the beam envelope function (black) with the interference fringes (grey). The beam size is changing over the longitudinal extent of the interference pattern; consequently, the measured rate of Compton scattering will be the average over the beam. This will dilute the measured modulation depth.

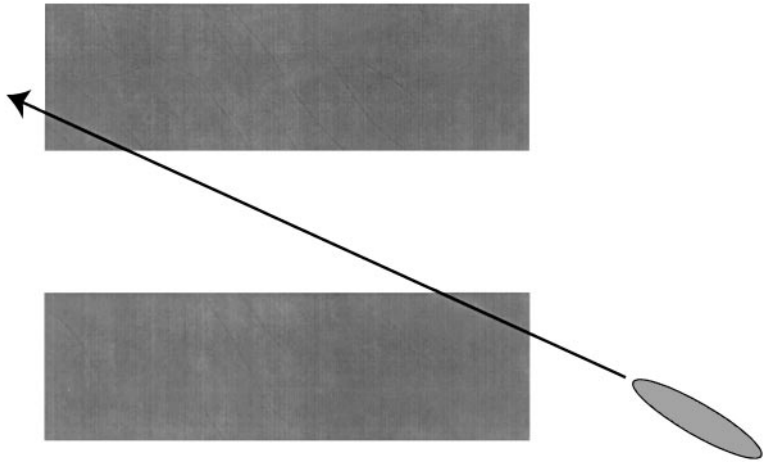

Figure 19 A beam passing through the interference pattern with a crossing angle. Because the beam passes through light and dark regions of the pattern, the measured modulation depth is reduced.

To measure the electron beam size with good accuracy, the laser beam size has to be smaller than half the betatron function. For $\sigma_z = \beta_y^*/2$, $\sigma_{\text{meas}} = 1.1\sigma_y$.

4.1.4 Laser Pathway Alignment Because the laser intensity is Gaussian distributed in x and z, it is important that the electron beam and the core of the two laser beams are centered at a common point in x and z.

In the case where one laser beam is aligned to the electron beam and the other is horizontally offset by δx, the effect on the modulation is given by

$$M_{\delta x} = \frac{2\exp\left(\frac{-\delta x^2}{4\sigma_{\text{L}}^2}\right)}{1+\exp\left(\frac{-\delta x^2}{2\sigma_{\text{L}}^2}\right)} M_{\text{ideal}}, \tag{24.}$$

where σ_{L} is the RMS transverse size of the laser. For an error $\delta x = \sigma_{\text{L}}/2$, this leads to a 0.2% degradation.

In the case where the two lasers are misaligned in z by an amount δz, the modulation becomes

$$M_{\delta z} = \exp\left(\frac{-\delta z^2}{8\sigma_z^2}\right) M_{\text{ideal}}. \tag{25.}$$

For an error of $\delta z = \sigma_z/2$, this results in a 3% degradation.

4.1.5 Spatial Coherence of the Laser If the spatial coherence of the laser is poor, the wavefronts will not be planar, resulting in a nonplanar interference pattern (Figure 20). This also reduces the measured modulation depth. In commercial high-power YAG lasers, the laser beam is sometimes designed to fully cover the

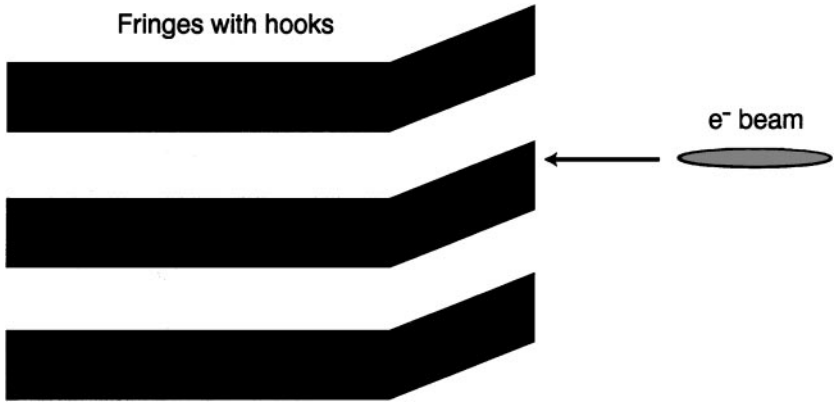

Figure 20 Effect of poor spatial coherence of the laser. The interference fringes become distorted in space, with "hooks" appearing on the fringes. These hooks tend to add intensity to the dark parts of the interference pattern, reducing the modulation depth.

YAG-rod in order to maximize output energy in the light pulse. However, part of the power is cut and reflected from the edge, resulting in poor spatial coherence (profile) due to interference with the main beam. This must be avoided, and in general the optics of the laser transport must be designed with care to preserve the spatial coherence of the transmitted power.

An additional concern is the spherical wavefront error. The focusing or diverging laser beam is formed by spherical waves (Figure 17). The spherical waves can only approximate plane waves (necessary to form a planar interference pattern) over a limited area around the focal point. The effect on modulation is given by

$$M_{\text{measure}} = \left(\frac{2}{\sqrt{1 + \frac{2\ln 2}{\pi} \frac{y}{z_R}}} - 1 \right) M_{\text{ideal}}. \tag{26.}$$

For a first-harmonic YAG laser focused to an RMS size of 40 μm, Equation 8 shows that z_R is 19 mm. At a distance of 2 mm from the focus point, therefore, $M_{\text{measure}} = 0.95 M_{\text{ideal}}$.

4.1.6 Temporal Coherence of the Laser Temporal coherence is essential for any kind of laser interferometry. If the coherence is poor, the fringe contrast is reduced. The modulation is given by

$$M_{\text{measure}} = \exp\left[-\pi \left(\frac{\delta\nu \Delta l}{c} \right)^2 \right] M_{\text{ideal}}, \tag{27.}$$

where $\delta\nu$ is the line width and Δl is the path difference in the two laser pathways from the beam splitter to the collision point. To obtain the ideal modulation, it is

necessary to choose a laser with a narrow line width or to equalize the path lengths in the interferometer design.

Another concern is the temporal profile of the laser pulse. The Nd:YAG laser has a wide natural line width, approximately 1 cm^{-1}. In Q-switch pulsed YAG lasers, many longitudinal modes are excited simultaneously, and interference of these modes generates sharp spikes in the output waveform. This increases the statistical scatter in the number of Compton-scattered photons.

In order to limit the number of longitudinal modes, injection seeding is essential. A frequency-stabilized solid-state laser injects a continuous low-power beam into the oscillator; when the Q-switch is opened, the high power beam starts from this coherent wave. Such devices are commercially available and can reduce the line width of a Nd:YAG laser to 0.03 cm^{-1}. The temporal profile becomes a Fourier-limited smooth waveform in this case.

4.1.7 Laser Jitter The laser-interferometer is subject to three forms of jitter that are significant on a shot-to-shot level: laser timing jitter, laser position jitter, and laser intensity jitter. Because the measurement of beam size takes many beam pulses, all forms of jitter must be controlled to acceptable levels. Note that laser jitter can cause a reduction in intensity in the dark regions of the interference pattern as well as the bright ones, and therefore it has the potential to reduce the measured beam size below the actual size.

High-powered lasers are usually operated in pulsed mode, and therefore they must be triggered such that the peak intensity of the laser light arrives at the IP at the same time as the electron beam. The jitter on laser triggering must be small relative to the length of the laser pulse.

Because the positioning of light and dark regions of the interference pattern is a function of the path lengths from the final mirrors of each pathway to the collision point, jitter of the incoming laser does not move the intensity pattern. However, the jitter can illuminate different parts of the pattern (Figure 21). Because the full modulation intensity is present only in a small region near the center of the pattern, this jitter must be small relative to the transverse laser size.

Finally, intensity jitter can change the apparent modulation depth by changing the overall intensity of the interference pattern when the electron beam passes through.

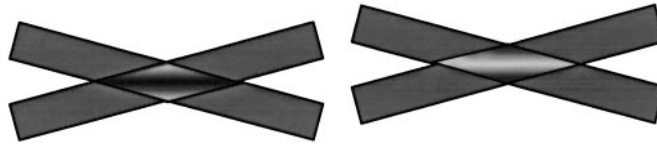

Figure 21 Effect of laser position jitter (or monitor installation jitter) on the interference pattern. The pattern does not move in space; however, the fringe that has the maximum intensity may change.

4.2 Laser-Interferometer Beam-Size Monitor in the Final Focus Test Beam

The Final Focus Test Beam (FFTB) is an experiment designed to test the optics and performance of a final focus system for future linear colliders. The FFTB beamline is located at the end of the SLAC linac and is designed to demagnify the incoming 46.6-GeV beam to an RMS size of 1.7 μm (horizontal) by 60 nm (vertical). The demagnification from the beam size in the linac required to do this is the same as the demagnification foreseen in some designs for future linear colliders (39).

A vertical beam size of 60 nm is clearly beyond the measurement capabilities of any technique described above other than laser interferometry. Although the horizontal size of 1.7 μm is measurable by conventional wire scanners, the product $\sigma_x\sigma_y$ is so small that, for the FFTB's nominal bunch charge of 1.0×10^{10} electrons, a conventional wire would be destroyed if it were hit by the full beam. Thus, a laser technique such as laser interferometry is also required for measurements of the larger horizontal size.

Figure 22 shows a schematic of the design selected for the FFTB's focal point. A single first-harmonic Nd:YAG laser is employed in three different operating modes. The first mode uses a 174° crossing angle to allow measurement of vertical beam sizes from 40 to 180 nm; the second mode uses a 30° crossing angle to allow measurement of vertical sizes from 160 to 720 nm; the third mode uses a 6° crossing angle in the horizontal, and can measure horizontal beam sizes from 0.76 to 3.4 μm (38). Figure 23 shows the modulation depths for each mode as a function of beam size. A total of six laser pathways enter the chamber where the collisions with the beam occur. For each mode, the lengths of the two pathways are equal, to guarantee perfect modulation. The final mirror that guides the light into the chamber is connected to remote-controlled movers with two degrees of freedom, which allow real-time alignment of the laser-beam positions at the IP. Initial alignment of the longitudinal position is performed using a slit with a z aperture of 500 μm, which is inserted into the laser pathway. Each laser in turn is directed onto the slit (by opening and closing appropriate shutters) and detected by a photodiode opposite the laser entry point; the z mover is adjusted to the center position of the transmitted window. Alignment of the lasers in x and y is done directly to the electron beam. The shutters are closed to allow light from only one of the six pathways into the interaction chamber, and the electron beam is steered across the laser beam. The distance from the nominal position of the electron beam to the position of peak Compton intensity is thus determined, and the laser light is then steered to the electron beam nominal position. This measurement also determines the relative intensity of each laser pathway, which in turn allows a correction for the unequal intensities, as discussed in the previous section.

The laser selected is a commercially available model that produces 200 mJ of energy and a 10-ns pulse length, with a repetition rate of 10 pulses per second. In order to improve the spatial profile, the oscillator mirror was selected to obtain

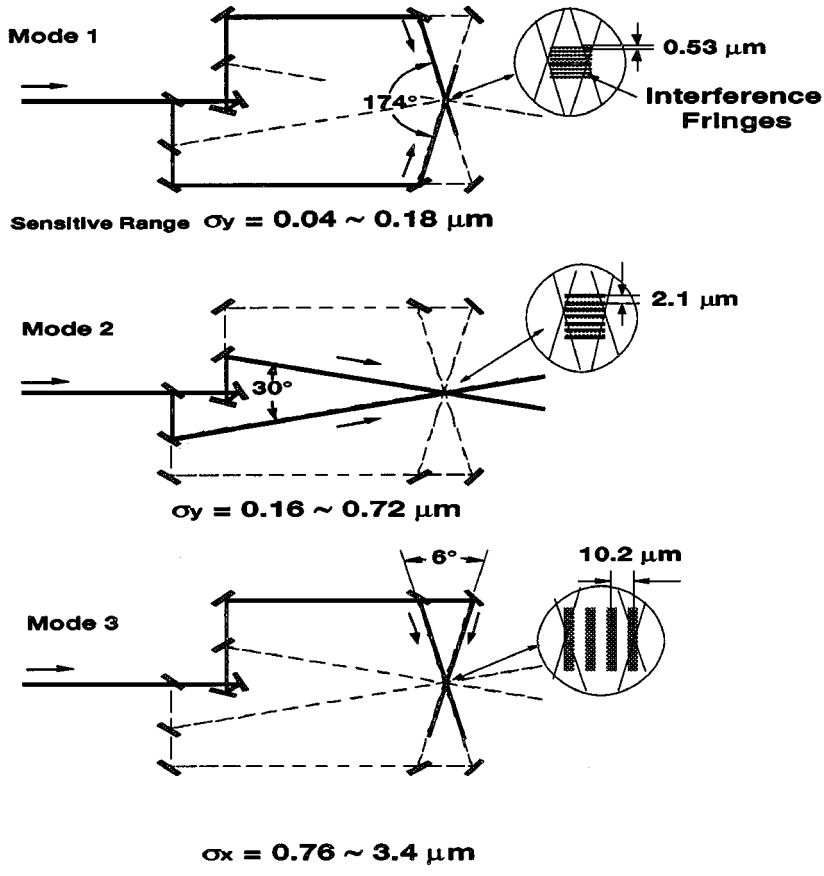

Figure 22 Diagram of the laser-interferometer beam-size monitor installed in the Final Focus Test Beam. Use of three different crossing angles allows measurement of both large and small vertical beam sizes, as well as horizontal sizes.

a smaller diameter in the YAG-rod. This provides a smooth Gaussian profile but reduces the power. The YAG laser oscillator is followed by an adjustable telescope that controls the beam size at the collision point. The laser pulse is then transmitted through a light pipe into the FFTB enclosure and into the interferometer apparatus. Each laser pathway contains a single lens with a focal length of 1 m, which is followed by the vacuum window into the collision chamber. Any high-frequency spatial component in the incoming laser beam creates an image far from the axis, and thus does not interact with the electron beam. Because the focal length of the final lens is long compared with the transverse size of the laser beam, third-order nonspherical distortions are negligible. Over the lifetime of the experiment, the laser size at the collision point was made as small as 25 μm and as large as

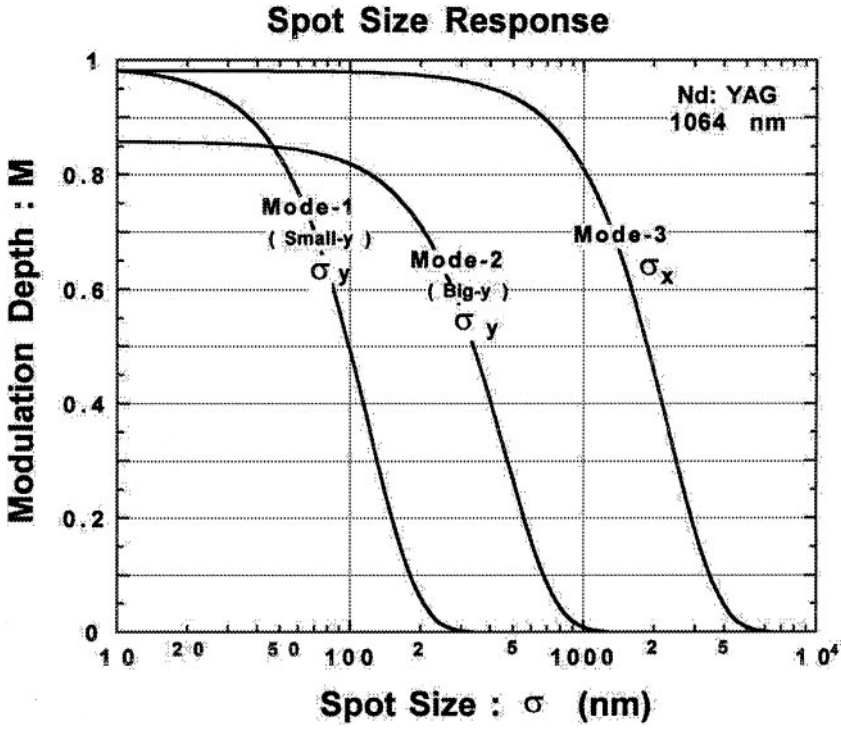

Figure 23 Modulation depth as a function of beam size for the three modes of the Final Focus Test Beam laser-interferometer beam-size monitor: crossing angles of 174, 30, and 6° are shown.

60 μm RMS. Although the 25-μm size results in better signal-to-noise performance and a reduced dilution due to the longitudinal size of the fringe pattern, it is more sensitive to alignment drifts. A compromise size of 40 μm was finally chosen. At the nominal bunch charge stated above, Equation 9 predicts a Compton flux of 850 photons for 40 μm RMS laser size. A splitter is used to direct 1% of the incident laser power to a charge-coupled device (CCD) camera; its image is sent to the accelerator control room as feedback to control the laser. The control room image allows users to verify that the laser spot is round, and the laser control system uses the digitized centroid position to control two mirrors that provide position feedback.

In the FFTB extraction line, the electron beam is separated from the γ-rays by a series of low-strength vertical bending magnets followed by a set of strong permanent magnet dipoles. A photomultiplier tube above the beamline downstream of the strong magnets detects the scattered photons, while a second detector below the beamline detects the degraded electrons. Ultimately, the photon detector is almost always used for the measurements. As Figure 8 shows, the electron spectrum contains a considerable contribution of particles that lose almost no energy and

are not ejected by the bends, and therefore the electron signal tends to be small compared with the photon signal.

One complication of the design is the considerable sensitivity to beam-induced backgrounds. The electron beam divergence at the focal point is quite large, and the apertures of nearby quadrupoles are tight. Unacceptable backgrounds can be generated by a small number of electrons hitting the vacuum pipe near the focal point. In general, the resulting beam loss is too small to detect with conventional loss monitors. The backgrounds are controlled through the use of special strong-focusing optics in the extraction line, steering near the focal point, and through the use of collimators in the last few hundred meters of the linac to eliminate beam halos (40), as well as a few adjustable collimators upstream in the FFTB.

Even with the careful attention to background suppression described above, some irreducible sources of beam-induced background remain, including the synchrotron radiation from the quadrupole magnets. Although the backgrounds are small relative to the peak signals (signal/noise ratio of 10 is routinely achieved), background counts tend to enhance the Compton signal when the beam passes through the nulls of the interference pattern and enlarge the measured size. This is corrected by triggering the laser at 10 Hz while the electron beam is run at 30 Hz. For each pulse with the laser present, the detected signal of the preceding and following pulses (with no laser present) is used to estimate the background. On each step of the beam position, 6 beam pulses with the laser and 12 pulses without the laser are combined to produce one reading. A full measurement of 50 steps of the beam position thus takes 900 pulses, or 30. Figure 24 shows a beam-size measurement without background subtraction and the same measurement with background subtraction.

4.3 Use of the Laser-Interferometer Beam-Size Monitor at the FFTB

Figure 25 shows a horizontal spot size measurement performed with the laser-interferometer set to its third mode. The modulation depth is $47.7 \pm 2.3\%$, corresponding to a beam size of 1.95 ± 0.06 μm.

Figure 26 shows a horizontal spot size measurement performed with the laser-interferometer set to its second mode, used for larger vertical spot sizes. The modulation depth is $82.6 \pm 2.9\%$, corresponding to a beam size of 90 nm. Note that the modulation depth is within the experimental error of the maximum achievable for this mode (86.6%).

Figure 27 shows a vertical spot size measurement performed with the laser-interferometer set to its first mode, used for the smallest vertical spot sizes. The modulation depth is 66%, corresponding to a beam size of 77 nm. The estimated statistical error on the beam-size measurement is 7 nm. Figure 28 shows the distribution of spot size measurements made over a three-day period in December 1997.

Achieving the smallest measured spot sizes requires a certain amount of "bootstrapping" because of the limited dynamic range of the vertical beam-size modes

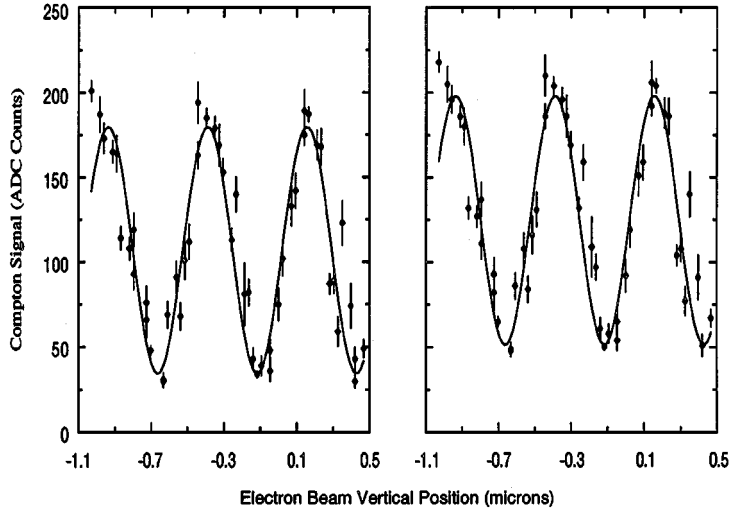

Figure 24 Beam-size measurement using 174° mode, both with (*left*) and without (*right*) subtraction of background. The decrease in modulation depth due to backgrounds causes the measured spot size to increase from 75 nm to 88 nm.

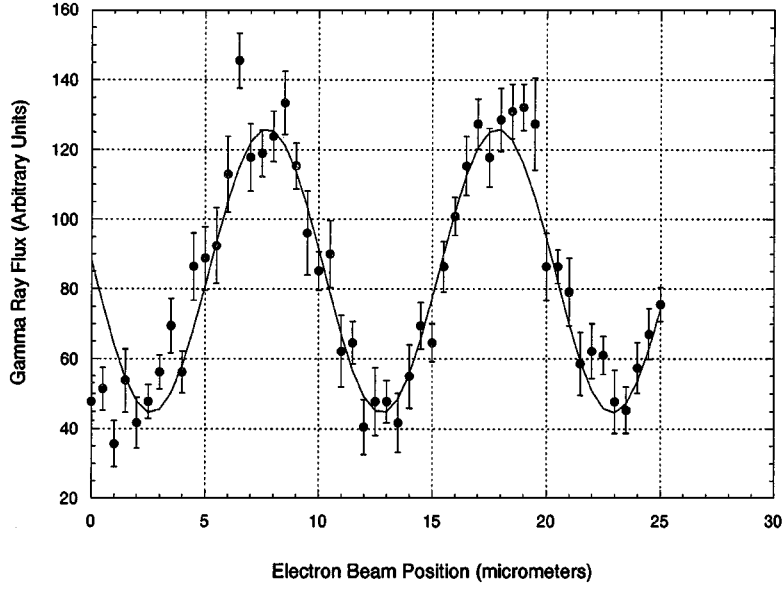

Figure 25 Horizontal beam-size measurement made with 6° mode. The measured Compton intensity (points) and sinusoidal fit (solid) are shown. Modulation depth is 47.7% $\pm$ 2.3%, corresponding to a beam size of 1.95 μm.

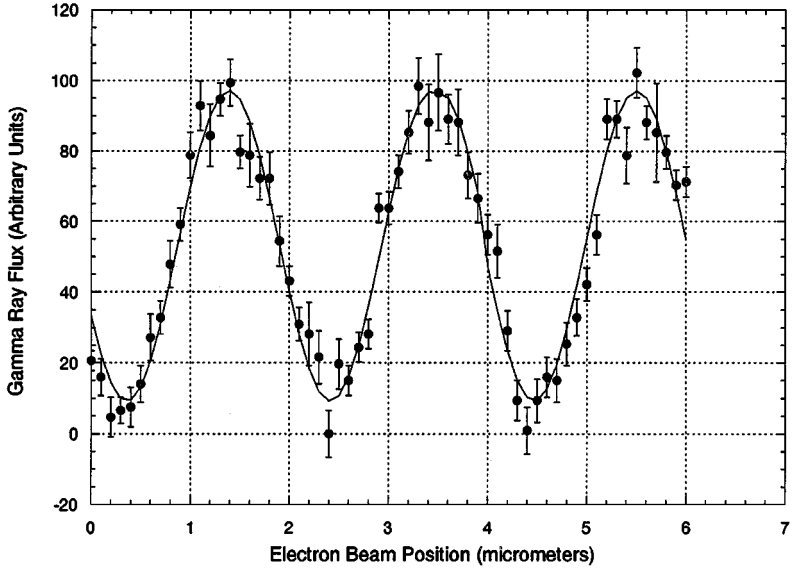

Figure 26 Vertical spot size measured with 30° mode. The modulation depth is 82.6% ± 2.9% corresponding to a beam size of 90 nm.

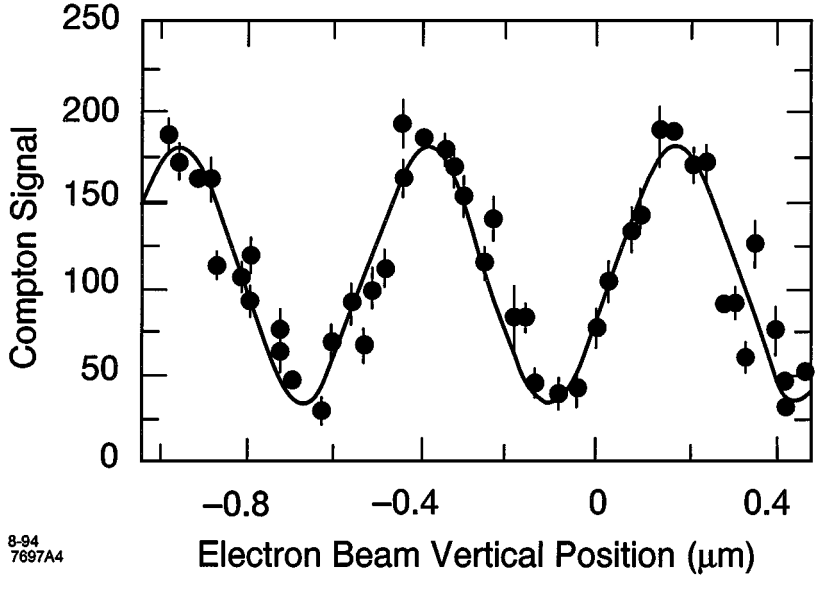

Figure 27 Vertical beam size measured with 174° mode. The modulation depth is 66%, corresponding to a beam size of 77 nm.

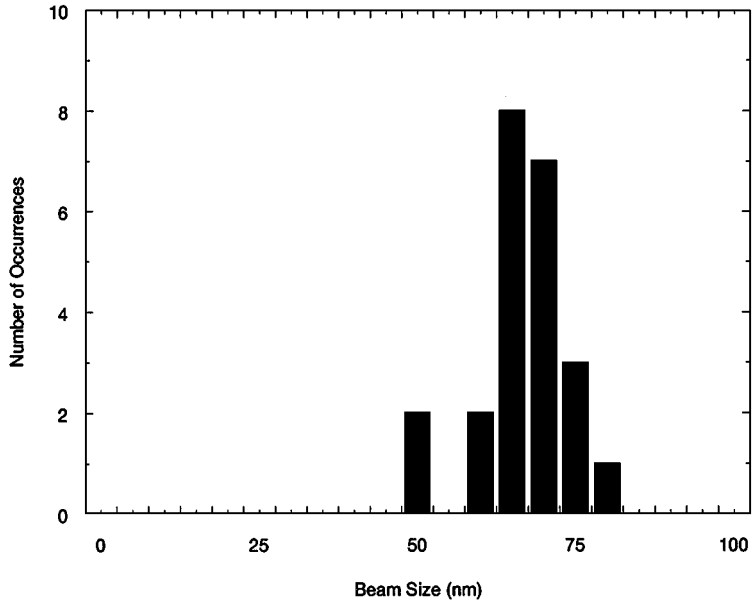

Figure 28 Distribution of 23 measurements made with the Final Focus Test Beam laser-interferometer beam-size monitor over a three-day period in December 1997.

and the large angular divergence of the electron beam. In general, if the waist position and the laser collision point differ by 0.5 mm in z, the beam is too large to measure with the smallest mode. Initially, the second measurement mode was set up and a difficult program of multidimensional parameter scanning was performed to achieve the first measurement of vertical size, after which the rest of the tuning proceeded quickly. In later periods, a high-resolution beam position monitor (BPM) near the IP (41) was used; the waist position and other aberrations were tuned to minimize the pulse-to-pulse jitter measured by the BPM, at which time the waist was moved by the distance from the BPM to the BSM. This procedure assumes that the jitter envelope and the beam envelope are reasonably similar in shape, which is not necessarily obvious; nonetheless, in practice, the procedure always converged quickly.

Although beam sizes as small as 58 nm were measured with the laser-interferometer, the focused electron beam size was typically measured to be 70 nm. Given the excellent performance of the SLAC linac during FFTB runs, the expected size was actually closer to 40 nm, even smaller than the design size. This is attributable, at least in part, to electron beam jitter at the focal point. The incoming jitter envelope has been measured, and its contribution to the expected jitter at the focal point is only 15 nm; nonetheless, direct measurements of the jitter indicate that the relative jitter between the beam and the fringe pattern are closer to 40 nm (42). This is consistent with the measured vibrations of the strong quadrupoles upstream of the focal point (caused by cooling water ground noise) and the predicted response of

the beam to these vibrations. The laser-interferometer is mounted on the table that supports the quadrupoles, but it is noted above that moving the laser and the interferometer relative to one another does not change the position of the bright and dark lines in the interference pattern. Thus, the beam was jittering while the interference pattern was fixed in its path. Options for correction of the jitter and/or direct measurement of same are under way.

4.4 Ultimate Limits of Laser-Interferometer Beam-Size Monitor Technique

The existing laser-interferometer installation was designed to meet the requirements of the FFTB experiment. Future projects, such as high-energy linear colliders, will have different requirements and will probably need to measure smaller spot sizes. At this time, variations on the laser-interferometer seem the best way to make such measurements.

The fundamental limit on the measured beam size is the wavelength of laser light. As described above, first-harmonic Nd:YAG lasers cannot be used for measurements below 40 nm. Frequency-doubled and frequency-tripled lasers are in common use today, and these would permit measurements down to 13 nm; the less common frequency-quadrupled lasers would conceivably permit measurement of beam sizes as small as 10 nm, and measurements of 20-nm spot sizes should be relatively easy to achieve. Such lasers would have a wavelength of 266 nm, well into the ultraviolet; this has significant implications for the availability of optics components and increases the risk of component damage.

Even a frequency-quadrupled laser will not permit direct measurement of the beam sizes required for some future linear colliders, which are projected to be as small as 3 nm. In addition, it will be difficult to make a laser-interferometer that can be installed at or near the IP of a linear collider, owing to interference with the particle physics detector. Such high-resolution BSMs are thus unlikely to be installed at the IP itself; rather, they would probably be placed at an upstream image point of the IP and would be used for tuning the beam.

The secondary limitation on beam-size measurement is the jitter discussed above. This can be overcome in two ways: Either eliminate the vibration of the magnets (via an optical anchor, for example), or measure the jitter with high-resolution BPMs and subtract its contribution to the beam size. For an image point of the IP, the jitter is likely to be less important, since there will not be strong quadrupole magnets in the vicinity.

5. CONCLUSIONS

A wide variety of technologies are available for the measurement of transverse sizes at high-energy charged particle beams. The simplest technique is a profile monitor, which can measure beam sizes down to a few tens of microns RMS and can perform a measurement on a single pulse. However, profile monitors are

invasive and subject to difficulties in image digitization. For beam sizes down to 1 μm, wire scanners are being used and can usually be made noninvasive. The primary drawbacks of wire scanners are long measurement times, more complex timing than in profile monitors, and the possibility of damaging the wire with the beam.

An unbreakable target for beam-size measurements are the photons in a laser, which are Compton scattered into the beam-forward direction. The most straightforward technique is to use a diffraction-limited, finely focused laser to take the place of a metal wire. Such "laser wire" scanners have been built and used to measure beam sizes down to 0.25 μm.

For still smaller sizes, one can use a laser to form an interference pattern in the path of the beam. The number of Compton-scattered photons are measured as a function of beam position in the interference pattern, and the modulation depth of the resulting sinusoidal distribution reveals the size of the electron beam. One such device, installed at the FFTB at SLAC, used a first-harmonic Nd:YAG laser ($\lambda = 1.064$ μm) to measure beam sizes down to 60 nm, with a theoretical ultimate resolution limit of 40 nm. Such a complex device requires considerable care in design and implementation to avoid deleterious systematic effects in the fringe pattern, but the FFTB monitor was repeatedly and reliably used for measuring beams with an RMS size under 100 nm.

Through use of second-, third-, or fourth-harmonic lasers, the achievable resolution can be improved, allowing 10-nm beam sizes to be measured. Such measurements will require improvements in the control or measurement of beam jitter induced by magnet vibration. These improved laser interferometers are foreseen as possible diagnostic tools in future linear colliders.

ACKNOWLEDGMENTS

The authors would like to acknowledge the assistance of the following people: at SLAC, D Burke, F-J Decker, C Field, R Iverson, D McCormick, M Ross, S Wagner, and D Walz; at KEK, K Oide and N Yamamoto; at KAWASAKI Heavy Industry, A Hayakawa and Y Ozaki. This work was supported by the Department of Energy under contract DE-AC03-76SF00515.

Visit the Annual Reviews home page at http://www.AnnualReviews.org

LITERATURE CITED

1. Neal RB, et al. *The Stanford Two-Mile Accelerator*. New York: Benjamin (1968)
2. Continuous Electron Beam Acceleration Facility. *CEBAF Design Report*. Newport News, VA: CEBAF (1986)
3. Stanford Linear Accelerator Center and Lawrence Berkeley Laboratory. *PEP Conceptual Design Report*. Stanford, CA: SLAC (1976)
4. LEP Study Group. *Design Study of a 15 to 100 GeV e^+e^- Colliding Beam Machine (LEP)*. Geneva: CERN (1978)

5. National Laboratory for High Energy Physics KEK. *TRISTAN Design Report I*. Tsukuba, Jpn.: KEK (1977)
6. Stanford Linear Accelerator Center. *SLC Design Handbook*. Stanford, CA: SLAC (1984)
7. LCLS Design Study Group. *LCLS Design Study Report*. Stanford, CA: SLAC (1998)
8. Ross MC, et al. *Proc. AIP Workshop Accel. Inst., 4th*, ed. JA Hinkson, G Stover. New York: AIP (1993)
9. Field C. *Nucl. Inst. Methods A* 360:467 (1995)
10. Carey DC. *The Optics of Charged Particle Beams*. Chur, Switzerland: Harwood (1987)
11. Wiedemann H. *Particle Accelerator Physics*. Berlin: Springer-Verlag (1993)
12. McDonald KT, Russell DP. In *Frontiers of Particle Beams: Observation, Diagnosis, and Correction*, ed. M Month, S Turner. New York: Springer-Verlag (1989)
13. Fewell N, Witkover R. *Proc. Proton Lin. Acc. Conf.*, ed. KH Harper, p. 51. Springfield, Virginia: Natl. Tech. Inf. Serv. (1972)
14. Raimondi P, et al. *Proc. 1998 Eur. Part. Accel. Conf. 6*, ed. S Myers et al, p. 245. Bristol, UK: Inst. Phys. Publ. (1998)
15. Raubenheimer T, Yokoya K. *Proposed ILC Parameters. LCC-Note-0003*. Stanford Linear Accel. Cent., Stanford, CA (1998)
16. Allison RW, et al. *A Radiation Resistant Chromium Activated Aluminum Oxide Scintillator*. *UCRL-19270*. Univ. Calif., Berkeley, CA (1969)
17. Bosser J, et al. *Nucl. Inst. Methods A* 238:45 (1985)
18. Graves WS, Johnson ED, Ulc S. *Proc. Beam Inst. Workshop 8*, ed. RO Hettel, SR Smith, JD Masek. New York: AIP (1998)
19. Yencho S, Walz D. *Proc. 1985 Part. Accel. Conf.* Piscataway, NJ: IEEE (1985)
20. Decker F-J, Brown R, Seeman JT. *Proc. 1993 Part. Accel. Conf.* Piscataway, NJ: IEEE (1993)
21. Gannon J, et al. *Proc. 1989 Part. Accel. Conf.* Piscataway, NJ: IEEE (1989)
22. Ross MC. *Proc. Workshop Accel. Inst. 2*, ed. ES McCrory. New York: AIP (1991)
23. McCormick D, et al. *Proc. Beam Inst. Workshop 6*, ed. GH Mackenzie, B Rawnsley, J Thomson. New York: AIP (1995)
24. Field C, McCormick D, Raimondi P, Ross M. *Proc. Beam Inst. Workshop 8*, ed. RO Hettel, SR Smith, JD Masek. New York: AIP (1998)
25. Bambade P, Erickson R. *Proc. 1986 Linear Accel. Conf.*, ed. F Bennett, J Kopta. Stanford, CA: SLAC (1986)
26. Raimondi P, Decker F-J. *Proc. 1995 Part. Accel. Conf*. Piscataway, NJ: IEEE (1996)
27. Seeman JT. *PEP-II Machine Advisory Committee Meeting, December 14–16, 1998*, ed. JT Seeman (1998)
28. Bovet C, et al. *Proc. Eur. Part. Accel. Conf. 5*, ed. S Myers, et al. Bristol, UK: Inst. Phys. Publ. (1996)
29. Emma P, Hendrickson LJ, Raimondi P, Zimmermann F. *Proc. 1997 Part. Accel. Conf.*, p. 452. Piscataway, NJ: IEEE Press (1999)
30. Brinkmann R. *Determination of HERA Specific Luminosity from Beam Separation Scans. DESY Tech. Note HERA 94-03*. Deutsches Elektronen-Synchrotron, Hamburg, Germany (1994)
31. Heitler W. *The Quantum Theory of Radiation*. Oxford, UK: Clarendon (1954)
32. Ginsburg IF, Kotkin GL, Serbo VG, Telnov VI. *Sov. J. Nucl. Phys.* 38(2):222 (1983)
33. Telnov VI. *Nucl. Inst. Methods A* 294:72 (1990)
34. Shintake T. *Nucl. Inst. Methods A* 311:453 (1992)
35. Ross MC, et al. *Proc. Beam Inst. Workshop 7*, ed. AH Lumpkin, CE Eyberger. New York: AIP (1997)
36. Kuhlman S, et al. *Physics and Technology*

of the Next Linear Collider. Stanford, CA: SLAC (1996)
37. Shintake T. *Proc. Beam Inst. Workshop 7*, ed. AH Lumpkin, CE Eyberger. New York: AIP (1997)
38. Shintake T, et al. *Proc. Int. Conf. High Energy Accel. 15*, ed. J Rossbach. Singapore: World Sci. (1993)
39. Oide K. *Proc. 1989 Part. Accel. Conf.* Piscataway, NJ: IEEE (1989)
40. Jacobsen R, et al. *Proc. 1991 Part. Accel. Conf.* Piscataway, NJ: IEEE (1992)
41. Slaton T, Mazaheri G, Shintake T. *Proc. 1998 Linear Accel. Conf.* Springfield, VA: Natl. Tech. Inf. Serv. (1999)
42. Woods M, Kotseroglou T, Shintake T. *Vertical Position Stability of the FFTB Electron Beam Measured by the KEK BSM. FFTB-Note 98-03*. Stanford Linear Accelerator Center, Stanford, CA (1998)